

Geometric effects in the Dyakonov–Shur theory of Terahertz photodetection

Riccardo Riolo, Marco Polini, Riccardo Mannella, and Andrea Tomadin

Dipartimento di Fisica dell'Università di Pisa, Largo Bruno Pontecorvo 3, I-56127 Pisa, Italy

Nonlinear resonances of plasma waves in field-effect transistors enable a well-known photodetection mechanism, first introduced by Dyakonov and Shur in the Nineties, especially suited to the Terahertz (THz) frequency range. Theoretical analyses of the mechanism always assume that the gate of the transistor, which is coupled to the antenna receiving the THz signal, is as long as the channel itself, at odds with typical experimental devices, where short gates are usually employed, e.g. due to fabrication constraints. In this work we overcome this limitation and provide a complete theory of Dyakonov–Shur photodetection in the presence of short gates. We develop our theory in such a general fashion that allows us to also treat the case in which multiple gates are present. We find that a sub-optimal positioning of the gates can substantially decrease the detection efficiency of the device and provide a compact analytical formula to quickly estimate the optimal gate position.

I. INTRODUCTION

Nonlinear effects in photonics and opto-electronics have been captivating a great deal of attention for decades [1, 2]. Typically, these nonlinearities stem from the intrinsic crystalline structure of the material under investigation, which determine its nonlinear polarization functions such as the second- and third-order ones. Another more subtle source of nonlinearity, however, stems from the motion of electrons in a crystal, in the so-called hydrodynamic transport regime [3]. As in classical fluid dynamics, these hydrodynamic nonlinearities are convection and the coupling of two collective variables, i.e. density and fluid-element velocity. Hydrodynamic effects in a system of electrons roaming in a crystal arise when electron-electron collisions take place on a time scale τ_{ee} that is much shorter than the time scale of the evolution of the above mentioned collective quantities. As the electrons move at the Fermi velocity v_F , the mean free path for electron-electron collisions is $\ell_{ee} = v_F \tau_{ee}$. In order to apply the hydrodynamic theory, ℓ_{ee} must be the shortest length scale in the system. In particular ℓ_{ee} must be shorter than the length L of the sample and shorter than the mean free path of electrons, determined by the scattering rate $1/\tau$ for collisions with phonons, impurities and defects, which do not conserve momentum.

In recent years, the realization of the hydrodynamic regime has been demonstrated in pure two-dimensional (2D) electron systems, where the parameters which control the time- and length-scales mentioned above can be easily tuned with the aid of metallic gates. Examples include graphene [4–11], GaAs/AlGaAs quantum wells [13–15], and the highly-pure Weyl semimetal WTe₂ [16].

The theory of hydrodynamic transport in graphene [17–23] shows some peculiarities due to the linear electron dispersion in the vicinity of the charge neutrality point, and changes qualitatively when the Fermi energy is smaller than the energy scale associated to the electron temperature [24, 25]. The scales of interest for the applicability of the hydrodynamic theory strongly depend on the density n and temperature T of the electron liquid. For both GaAs [26] and single-layer

graphene [27, 28], the inverse lifetime of a quasiparticle of energy ε_k , in the limit $|\varepsilon_k - \varepsilon_F| \ll k_B T \ll \varepsilon_F$, ε_F being the Fermi energy, scales with temperature as $1/\tau_{ee} \propto -T^2 \ln T$.

What are the implications of hydrodynamic electron transport on the fabrication of a device of some use in applications? The first device of practical interest was proposed theoretically by Dyakonov and Shur (DS) in the Nineties [29–32]. DS considered a field-effect transistor (FET) where the 2D electron fluid in the channel is in the hydrodynamic transport regime. This device can be used as a THz photodetector [31] by connecting an antenna to the source and gate contacts. Indeed, a DC potential (the *photovoltage*) is established between source and drain when the FET is driven by an AC signal, which is thus *rectified*. The underlying mechanism involves the generation and propagation of electron density waves (*plasma waves*) [29–34], which mix because of the hydrodynamic nonlinearities. For the plasma waves to be described by the hydrodynamic model, however, their frequency ω must be much shorter than the electron-electron collision rate $1/\tau_{ee}$. This “collisional” regime is the opposite of the usual “collisionless” regime of plasmons [26], where electrons can be understood to move freely under the action of a collective field. For GaAs at $n = 10^{11} \text{ cm}^{-2}$, $T = 10 \text{ K}$, the scattering length is $\ell_{ee} \sim 200 \text{ nm}$ and the maximum frequency of plasma waves $f_{\text{max}} \sim 100 \text{ GHz}$. On the other hand, for single-layer graphene (SLG) at $n = 10^{12} \text{ cm}^{-2}$, $T = 200 \text{ K}$, they are $\ell_{ee} \sim 200 \text{ nm}$ and $f_{\text{max}} \sim 1 \text{ THz}$, respectively. DS theory predicts a frequency-resolved detection for a sufficiently clean channel, i.e. when the frequency ω is larger than the scattering rate $1/\tau$.

The DS rectification mechanism is of practical importance in the detection of electromagnetic radiation in the THz range because frequencies in this range exceed the cutoff frequency of electronics circuitry, and other devices based on e.g. Schottky barriers, photothermoelectric or photogalvanic effects [40] offer limited bandwidth or need cryogenic temperatures. The original theory of DS detection dealt with a parabolic-band 2D electron system as the one that can be found in a GaAs electron-doped quantum well but has been extended to devices based on

SLG [33] and bilayer graphene [34], where plasma waves at typical electron densities fall naturally in the THz range and ultra-high electron mobilities at room temperature reduce the minimum frequency necessary for frequency-resolved detection. Similarly, experiments in DS photodetection first used FETs based on GaAs heterostructures [35] and then graphene-based devices [36–38]. Resonant, frequency-resolved detection was finally measured in bilayer graphene in 2018 in the pioneering experiments by Bandurin et al. [39].

Notwithstanding this multi-decade-long research activity in DS photodetection, most theoretical works deal with very simple geometries, where a single gate occupies the entire length of the FET channel. However, in a typical experimental setup, the width of the employed gates often tends to be much shorter than the channel length [36, 37] due to fabrication constraints. As a consequence, the position of the gate between source and drain becomes a new geometrical parameter that has to be determined before fabrication on the basis of some criterion (for example, in order to maximize the photodetector efficiency). In this work, we systematically address for the first time how the gate length and its precise positioning affect the photovoltage. Moreover, motivated by current fabrication possibilities, we additionally study the effects of *multiple* gates in a single FET.

Our Article is organized as following. In Sec. II, we review the theory of electron hydrodynamics for both GaAs and SLG. In Sec. III, we discuss the electrostatics of a device with an arbitrary number of top gates and the boundary conditions needed in order to operate as a detector. In Sec. IV, we calculate the photovoltage. We discuss the plasma-waves solution of the hydrodynamic equations and then the second-order solution leading to the DC signal. Moreover, we provide an approximate formula in the limit of a single gate of negligible width. Finally, a summary of our main results and a brief set of conclusions are reported in Sec. V.

II. BRIEF RECAPITULATION OF HYDRODYNAMIC THEORY

In the hydrodynamic regime, electron-electron scattering is the process which is responsible for the local equilibration of the electron system. Within the kinetic theory approach [41], the electron system can be described by the distribution function $f_{\lambda\mathbf{k}}(\mathbf{r}, t)$, which measures the probability that an electron with wave vector \mathbf{k} and belonging to band λ is found in the neighborhood of position \mathbf{r} at time t . The explicit form of the probability distribution function in a state of quasi-equilibrium (i.e. when thermodynamic quantities are locally well-defined, but might vary in space and time) is obtained by requiring that the collisional integral for electron-electron scattering in the Boltzmann equation vanishes [42–44]. Assuming that the electron dispersion is isotropic, the probability distribution depends only on

the magnitude k of the wave vector or, equivalently, on the single-particle state energy $\varepsilon_{\lambda k}$. In the following, we will also assume that the 2D system is inhomogeneous in the x direction only (this will be the source-drain direction when applying the theory to a FET in the DS setup). The result is that $f_{\lambda k}$ is a drifted Fermi-Dirac distribution,

$$f_{\lambda k}(x, t) = \left(\exp \frac{\varepsilon_{\lambda k} - \hbar v(x, t)k - \mu(x, t)}{k_{\text{B}}T} + 1 \right)^{-1}, \quad (1)$$

where $v(x, t)$ is the local drift velocity, $\mu(x, t)$ the local chemical potential, and T the temperature. We shall assume throughout this work that the temperature is much smaller than the Fermi temperature, i.e. $T \ll T_{\text{F}}$. In such limit, the distribution (1) becomes the zero-temperature Fermi-Dirac distribution. Thus there is a local Fermi energy $\varepsilon_{\text{F}}(x, t)$, with a Fermi wavevector $k_{\text{F}}(x, t)$ that smoothly depends on x and t through the local density $n(x, t)$,

$$k_{\text{F}}(x, t) = \sqrt{\frac{4\pi n(x, t)}{g}}, \quad (2)$$

where g is the degeneracy of single-particle states.

The hydrodynamic equations are obtained from the Boltzmann kinetic equation by considering the moments of the distribution function, i.e. the density and drift velocity

$$n_{\lambda}(x, t) \equiv \frac{1}{L^2} \sum_{\mathbf{k}} f_{\lambda\mathbf{k}}(x, t) \quad (3)$$

$$\mathbf{v}_{\lambda}(x, t) \equiv \frac{1}{L^2} \sum_{\mathbf{k}} f_{\lambda\mathbf{k}}(x, t) \nabla_{\mathbf{k}} \varepsilon_{\lambda\mathbf{k}}. \quad (4)$$

The first hydrodynamic equation is the continuity equation, which expresses the conservation of the particle number. The second hydrodynamic equation is the Navier-Stokes equation, which expresses the conservation of momentum. By assuming a uniform temperature T , there is no heat transport, therefore we can neglect the thermal transport equation, which expresses the conservation of energy. The actual form of the hydrodynamic equations depends on the electronic dispersion in the material that hosts the 2D electron gas, and has been discussed e.g. in Ref. [42].

Dissipative effects in hydrodynamic theory are characterized by three transport coefficients [41, 45]: the shear viscosity, which describes the friction between layers of fluid moving with different velocities; the bulk viscosity, which describes the dissipation due to a compression or expansion of the liquid; and the thermal conductivity, which describes the dissipation of energy due to temperature gradients. In the low-frequency hydrodynamic limit, the bulk viscosity vanishes [26, 46], while the kinematic shear viscosity for both GaAs [26] and graphene [46] is $\nu = \nu_{\text{F}} \ell_{\text{ee}}/4$. The interactions of the electrons with

phonons or impurities, which tend to restore the equilibrium distribution $f_k^{(\text{eq})}$, are included in the theory with the so-called relaxation-time approximation, which adds the term $-(f_k(x, t) - f_k^{(\text{eq})})/\tau$ to the Navier-Stokes equation. Here, the phenomenological parameter τ represents the characteristic time scale over which the momentum of a fluid element is randomized.

The hydrodynamic equations relate the density n , the drift velocity v , the electrostatic potential φ and the pressure of the electron gas P . Therefore, alongside these two equations, we need two constitutive relations: the solution to the electrostatic problem, which provides the relation $\varphi(n)$, and the equation of state $P(n)$, which is dependent on the electron dispersion. We now report the hydrodynamic equations for both 2D parabolic-band electron systems (GaAs being the cleanest example in terms of electronic mobility) and SLG, following Refs. [42–44].

A. Gallium arsenide

Conduction-band electrons in n -doped GaAs have a parabolic dispersion

$$\varepsilon_k = \frac{\hbar^2 k^2}{2m}, \quad (5)$$

where m is the band mass, whose value for GaAs is $m \approx 0.063m_e$, where m_e is the bare electron mass in vacuum. The degeneracy factor is $g = 2$ and is solely due to the electron's spin.

The continuity equation reads as following,

$$\partial_t n + \partial_x(nv) = 0, \quad (6)$$

while the Navier–Stokes equation is

$$\partial_t v + v\partial_x v = \frac{e\partial_x \varphi(n)}{m} - \frac{\partial_x P(n)}{nm} - \frac{v}{\tau} + \nu\partial_x^2 v, \quad (7)$$

where τ is the momentum relaxation time and ν the kinematic viscosity. In the limit $T \ll T_F$, the equation of state reads

$$P(n) = \frac{n\varepsilon_F(n)}{2} = \frac{\hbar^2 \pi n^2}{2m}. \quad (8)$$

Inserting this result into the Navier–Stokes equation we find

$$\partial_t v + v\partial_x v = \frac{e\partial_x \varphi(n)}{m} - \frac{\pi\hbar^2 \partial_x n}{m^2} - \frac{v}{\tau} + \nu\partial_x^2 v. \quad (9)$$

B. Single-layer graphene

Electrons in SLG, in the vicinity of the charge neutrality point, have a linear dispersion

$$\varepsilon_{\lambda k} = \lambda\hbar v_F k, \quad (10)$$

where $v_F \approx 10^8$ cm/s is the Fermi velocity and $\lambda = \pm$ for the conduction and valence band, respectively [47]. Twofold spin and valley degeneracies yield $g = 4$.

The continuity equation takes the same form as in GaAs

$$\partial_t n + \partial_x(nv) = 0, \quad (11)$$

where $n(x, t) = n_+(x, t) + n_-(x, t)$ is total number density. In the limit in which the drift velocity is much smaller than the Fermi velocity, $v(x, t) \ll v_F$, the Navier–Stokes equation is [33]

$$\begin{aligned} \frac{3P}{v_F^2} \left(\partial_t v + v\partial_x v - \frac{v\partial_t n}{n} + \frac{v}{\tau} - \nu\partial_x^2 v \right) + \frac{3v}{v_F^2} \partial_t P \\ = -\partial_x P + (n_+ - n_-)e\partial_x \varphi(n). \end{aligned} \quad (12)$$

In the limit $T \ll T_F$, the equation of state reads

$$P(n) = \frac{n\varepsilon_F(n)}{3} = \frac{\pi^{1/2}\hbar v_F n^{3/2}}{3}. \quad (13)$$

Away from the charge neutrality point, i.e. for a small hole population $n_- \ll n_+ \approx n$, the Navier–Stokes equation reduces to the simpler form

$$\partial_t v + v\partial_x v = \frac{v_F^2 e \partial_x \varphi(n)}{\varepsilon_F(n)} - \frac{v_F^2 \partial_x n}{2n} - \frac{v\partial_t n}{2n} - \frac{v}{\tau} + \nu\partial_x^2 v. \quad (14)$$

III. GEOMETRY OF THE DEVICE

A. Electrostatics of a single-gated and dual-gated transistor

The FET channel that hosts the 2D electron liquid lies in the plane $z = 0$ and extends along the x direction for a total length L . Throughout this work we will assume that the device is translationally invariant in the y direction. The source and drain contacts are connected to the two extrema of the channel, as shown schematically in Fig. 1. We model the top and bottom gate as two perfect conductors lying in the planes $z = h_t$ and $z = -h_b$, respectively. The dielectric constant of the medium surrounding the channel is ε_t for $0 < z < h_t$ and ε_b for $-h_b < z < 0$. External voltage generators fix the electric potential of the top and bottom gates to the values V_t and V_b , respectively, while the electric potential $\varphi(x)$ in the channel is not homogeneous and is determined by the hydrodynamics and constitutive equations, as discussed above.

As discussed in the Introduction, in this work we consider a device in which the top gate only partially extends over the channel. The bottom gate, on the contrary, extends over the whole channel from source to drain. With this configuration in mind, we distinguish between the regions of the x axis where only the bottom gate is present,

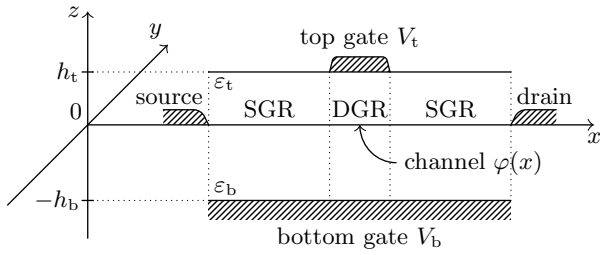


FIG. 1. Schematics of a FET with a single top gate. The channel lies on the plane $z = 0$ and the system is translationally invariant along the y direction. The dielectric constant is ϵ_t (ϵ_b) and the gate layer thickness is h_t (h_b) above (below) the channel. The channel region where both the top and the bottom gates are present is denoted dual-gated region (DGR) while the rest are denoted single-gated regions (SGRs). The electric potential in the channel, top, and bottom gate is $\varphi(x)$, V_t , and V_b , respectively.

called *single-gated regions* (SGRs), and the regions where both gates are present, called *dual-gated regions* (DGRs).

If the distances h_t , h_b between the gates and the channel are much smaller than the length scale on which the electron density varies, then the relation between the electric potential and the density assumes a local form. In this *local capacitance approximation* [29–34], the electric field is directed along the z direction, $E_z(x, z)$. (Here we neglect the fringe field due to the finite dimension of the gate conductors.) The electric displacement field is $D_z(x, z) = \epsilon(z)E_z(x, z)$. From Gauss' law $\partial_z D_z(x, z) = -4\pi e\delta(z)n(x)$ we find the relation between the displacement field on opposite sides of the channel

$$D_z(x, z = 0^+) - D_z(x, z = 0^-) = -4\pi en(x). \quad (15)$$

The electric displacement field above the channel depends on whether x is in the SGRs or in the DGR,

$$D_z(x, z = 0^+) = \begin{cases} 0, & \text{if } x \in \text{SGRs}, \\ -\frac{\epsilon_t(V_t - \varphi(x))}{h_t}, & \text{if } x \in \text{DGRs}, \end{cases} \quad (16a)$$

while the field below the channel is the same in every region

$$D_z(x, z = 0^-) = \frac{\epsilon_b(V_b - \varphi(x))}{h_b}. \quad (16b)$$

The relation between the electron density in the channel and the electric potentials depends on the region,

$$en(x) = \begin{cases} C_b(V_b - \varphi(x)), & \text{if } x \in \text{SGRs}, \\ C_b(V_b - \varphi(x)) + C_t(V_t - \varphi(x)), & \text{if } x \in \text{DGRs}, \end{cases} \quad (17)$$

where C_t and C_b are the geometrical capacitances per unit area associated to top and bottom gate, respectively,

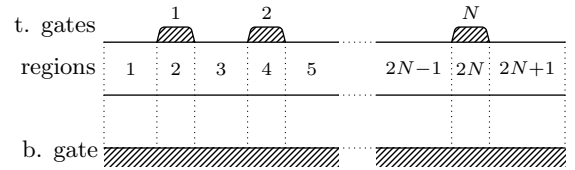


FIG. 2. Schematics of a FET configuration with N top gates. We number the regions below and between the gates with an index $j = 1, \dots, 2N + 1$, so that the regions with j odd (even) are SGRs (DGRs).

given by

$$C_{t,b} = \frac{\epsilon_{t,b}}{4\pi h_{t,b}}. \quad (18)$$

Finally, we generalize the previous discussion to a geometry with several top gates, as shown in Fig. 2. Let us consider the case of N top gates, which divide the channel into $2N + 1$ regions, each of length ℓ_j , with $j = 1, 2, \dots, 2N + 1$, so that $\sum_j \ell_j = L$. We denote the density and electric potential in the j -th region by $n^{(j)}(x, t)$ and $\varphi^{(j)}(x, t)$, respectively, where the spatial coordinate x varies in the interval $(0, \ell_j)$. With this numbering convention, the *odd* regions are SGRs, while the *even* regions are DGRs. The average electron density n_0 in the channel is determined by the voltage applied to the bottom gate, which occupies the whole length of the device, according to the relation $n_0 = C_b V_b / e$.

B. Dyakonov–Shur boundary conditions

The THz radiation, collected by the lobes of the antenna, is funneled into the FET contacts and determines the electric potential difference between the source contact and the top gates. For definiteness, we assume that the source contact is grounded and that the voltage $V_t(t)$ common to all the top gates oscillates with the frequency ω of the incoming radiation and with an amplitude U_a , which depends on implementation details such as the efficiency of the antenna and its impedance matching with the FET. Moreover, the DS scheme requires that the drain contact is floating, so that the current density $j(x, t) = n(x, t)v(x, t)$ vanishes at $x = L$. These requirements provide the following Dyakonov–Shur boundary conditions that complement the hydrodynamic and constitutive equations discussed above:

$$\varphi^{(1)}(0, t) = 0, \quad (19a)$$

$$V_t(t) = U_a \cos(\omega t), \quad (19b)$$

$$j^{(2N+1)}(\ell_{2N+1}, t) = 0. \quad (19c)$$

IV. CALCULATION OF THE PHOTOVOLTAGE

A. Perturbative expansion

The photovoltage is the DC component of the electric potential difference between source and drain

$$\Delta U = \langle \varphi^{(1)}(0, t) - \varphi^{(2N+1)}(\ell_{2N+1}, t) \rangle_t, \quad (20)$$

where $\langle a(t) \rangle_t$ denotes the time average of the oscillating signal $a(t)$,

$$\langle a(t) \rangle_t \equiv \frac{\omega}{2\pi} \int_0^{2\pi/\omega} a(t) dt, \quad (21)$$

where ω is its angular frequency. Since the full hydrodynamic equations are not amenable to an analytical solution, to calculate the photovoltage we follow the DS procedure [31], which consists in a perturbative expansion up to the second order in the amplitude U_a of the voltage oscillation produced by the incoming radiation.

For both GaAs and SLG, taking into account the boundary conditions in Eq. (19a), the steady solution of the hydrodynamic equations is

$$v(x, t) = 0, \quad \varphi(x, t) = 0, \quad n(x, t) = n_0. \quad (22)$$

Due to the nonlinearities in Eqs. (6), (9), (11), and (14), a perturbative, monochromatic drive of frequency ω generates oscillations at all the harmonics of ω , including a DC component at zero frequency. Expanding around the steady state defined by Eq. (22), up to the second order in the amplitude U_a , we seek solutions of the form

$$v(x, t) = v_1(x, t) + v_2(x, t) + \delta v(x), \quad (23a)$$

$$\varphi(x, t) = \varphi_1(x, t) + \varphi_2(x, t) + \delta \varphi(x), \quad (23b)$$

$$n(x, t) = n_0 + n_1(x, t) + n_2(x, t) + \delta n(x), \quad (23c)$$

where all the quantities with subscript l oscillate at frequency $l\omega$ and are proportional to $(U_a)^l$, while δv , $\delta \varphi$, δn are the DC components of the second order. This expansion leads to a set of linear equations of the first order and a set of the second order, which depends on the solution of the former. Therefore, in order to calculate the photovoltage ΔU , i.e. the DC component of the second order, we now proceed to solve the first-order equations.

B. First-order solution: plasma waves

The local capacitance approximation in Eq. (17), at the first order in U_a , becomes

$$en_1^{(j)} = \begin{cases} -C_b \varphi_1^{(j)}, & \text{for odd } j, \\ -(C_b + C_t) \varphi_1^{(j)} + U_a \cos \omega t, & \text{for even } j. \end{cases} \quad (24)$$

The first-order hydrodynamic equations are equal in form for both GaAs and SLG

$$\partial_t n_1 + n_0 \partial_x v_1 = 0, \quad (25)$$

$$\partial_t v_1 = \frac{e}{m} \partial_x \left(\varphi_1 - \frac{en_1}{C_q} \right) - \frac{v_1}{\tau} + \nu \partial_x^2 v_1. \quad (26)$$

In the last equation, the effective mass m corresponds to the band mass for GaAs and to the density-dependent cyclotron mass

$$m = \frac{\hbar k_F(n_0)}{v_F} \quad (27)$$

for SLG. The parameter C_q , which comes from the pressure term in the Navier–Stokes equation, is a capacitance per unit area which is given by the following constant value for GaAs

$$C_q = \frac{me^2}{\pi \hbar^2}, \quad (28)$$

and by

$$C_q = \frac{2e^2 n_0}{\varepsilon_F(n_0)} \quad (29)$$

for SLG. Here, the density-dependence can be understood as a *quantum capacitance* effect [48], i.e. a non-linear dependence of the electric potential on the charge density $-en_0$.

We now eliminate the electric potential from Eq. (26) by using the local capacitance approximation in Eq. (24), i.e. by substituting

$$\varphi_1^{(j)} - \frac{en_1^{(j)}}{C_q} = \begin{cases} -\frac{en_1^{(j)}}{C_j}, & \text{for odd } j, \\ -\frac{en_1^{(j)}}{C_j} + \frac{C_t U_a \cos \omega t}{C_b + C_t}, & \text{for even } j, \end{cases} \quad (30)$$

where we have introduced the effective capacitances C_j ,

$$C_j^{-1} = \begin{cases} C_1 \equiv C_b^{-1} + C_q^{-1}, & \text{odd } j, \\ C_2 \equiv (C_b + C_t)^{-1} + C_q^{-1}, & \text{even } j. \end{cases} \quad (31)$$

The linearized hydrodynamic equations describe “plasma waves” [29–34], which, in this formalism and as DS noted, are analogous to surface waves in shallow water [45]. To find the spatial dispersion of plasma waves we consider the homogeneous system of equations

$$\begin{pmatrix} -i\omega & ik_x n_0 \\ e^2 ik_x / m C_j & -i\omega + \tau^{-1} + \nu k_x^2 \end{pmatrix} \begin{pmatrix} n_1^{(j)}(k_x, \omega) \\ v_1^{(j)}(k_x, \omega) \end{pmatrix} = 0. \quad (32)$$

There are two modes with wave vectors $\pm K_j(\omega)$, which depend on the region, with

$$K_j(\omega) = \sqrt{\frac{\omega^2 + i\omega/\tau}{s_j^2 - i\omega\nu}}. \quad (33)$$

Here, s_j is the speed of plasma waves in the j -th region,

$$s_j = \sqrt{\frac{eV_b C_b}{m C_j}}. \quad (34)$$

The first-order solutions are harmonics with the same frequency ω of the driving voltage, i.e.

$$n_1^{(j)}(x, t) = n_1^{(j)}(x, \omega)e^{-i\omega t} + cc, \quad (35a)$$

$$v_1^{(j)}(x, t) = v_1^{(j)}(x, \omega)e^{-i\omega t} + cc, \quad (35b)$$

where each component is the superposition of two modes:

$$n_1^{(j)}(x, \omega) = n_0 (A_{2j-1}e^{iK_j x} + A_{2j}e^{-iK_j x}), \quad (36a)$$

$$v_1^{(j)}(x, \omega) = \frac{\omega}{K_j} (A_{2j-1}e^{iK_j x} - A_{2j}e^{-iK_j x}). \quad (36b)$$

The $(4N+2)$ coefficients A_l are fixed by the two boundary conditions in Eq. (19a) and by $4N$ conditions that match the solutions between any two adjacent regions of the channel. The two boundary conditions at first order read

$$\varphi_1^{(1)}(0, \omega) = 0, \quad v_1^{(2N+1)}(\ell_{2N+1}, \omega) = 0. \quad (37)$$

A set of $2N$ matching conditions comes from integrating Eq. (25) along an infinitesimal interval centered on a generic point x . It follows that $v_1(x, \omega)$ is continuous in x , i.e.

$$v_1^{(j)}(\ell_j, \omega) = v_1^{(j+1)}(0, \omega). \quad (38)$$

The other $2N$ conditions analogously come from Eq. (26), which implies the continuity in x of

$$\varphi_1(x, \omega) - \frac{en_1(x, \omega)}{C_q} + \nu \partial_x v_1(x, \omega). \quad (39)$$

Rewriting it in terms of n_1 , the conditions are

$$\left(\frac{C_b}{C_1} - \frac{i\omega\nu}{s^2}\right) \frac{n_1^{(j)}(\ell_j, \omega)}{n_0} = -\frac{C_t}{C_b + C_t} \frac{U_a}{2V_b} + \left(\frac{C_b}{C_2} - \frac{i\omega\nu}{s^2}\right) \frac{n_1^{(j+1)}(0, \omega)}{n_0}, \quad \text{odd } j, \quad (40a)$$

$$\left(\frac{C_b}{C_2} - \frac{i\omega\nu}{s^2}\right) \frac{n_1^{(j)}(\ell_j, \omega)}{n_0} - \frac{C_t}{C_b + C_t} \frac{U_a}{2V_b} = \left(\frac{C_b}{C_1} - \frac{i\omega\nu}{s^2}\right) \frac{n_1^{(j+1)}(0, \omega)}{n_0}, \quad \text{even } j, \quad (40b)$$

where $s^2 = eV_b/m$. As the frequency ω is fixed by the antenna, Eqs. (37), (38), and (40) provide a linear system of $(4N+2)$ equations for the coefficients A_l appearing in Eq. (36).

In the hydrodynamic regime, the electronic mobility has a correction to the ohmic value $\mu = e\tau/m$, due to the pressure of the electron fluid. The mobility relates the electron velocity to the electric field, $v = \tau \partial_x \varphi$. Thus,

considering the stationary state of Eq. (26), the electron mobility assumes different values between the SGRs and DGRs,

$$\mu_j = \begin{cases} \frac{e\tau}{m} \left(1 + \frac{C_b}{C_q}\right), & \text{odd } j, \\ \frac{e\tau}{m} \left(1 + \frac{C_b + C_t}{C_q}\right), & \text{even } j. \end{cases} \quad (41)$$

C. Second-order solution: DC photovoltage

Since we are interested in the calculation of the DC signal ΔU , we take the time average of the second-order equations. The local capacitance approximation (17) becomes

$$e\delta n^{(j)} = \begin{cases} -C_b \delta \varphi^{(j)}, & \text{odd } j, \\ -(C_b + C_t) \delta \varphi^{(j)}, & \text{even } j. \end{cases} \quad (42)$$

The time-averaged second-order hydrodynamic equations read

$$\begin{aligned} \langle \partial_x (n_1 v_1) \rangle_t + n_0 \partial_x \delta v &= 0, \quad (43) \\ \langle v_1 \partial_x v_1 \rangle_t &= \frac{e}{m} \partial_x \left(\delta \varphi - \frac{e\delta n}{C_q} \right) - \frac{\delta v}{\tau} + \nu \partial_x^2 \delta v \\ &\quad - \eta \left\langle \frac{e}{m} \frac{n_1}{n_0} \partial_x \varphi_1 - v_F^2 \frac{n_1 \partial_x n_1}{n_0^2} + \frac{v_1 \partial_t n_1}{n_0} \right\rangle_t, \quad (44) \end{aligned}$$

where the parameter η distinguishes between the two cases

$$\eta = \begin{cases} 0, & \text{GaAs,} \\ \frac{1}{2}, & \text{SLG.} \end{cases} \quad (45)$$

Taking into account the boundary condition at the drain, the continuity equation becomes

$$\langle n_1 v_1 \rangle_t + n_0 \delta v = 0. \quad (46)$$

By using the first-order Eqs. (25) and (26), we can rearrange the expression for the DC component as

$$\begin{aligned} \frac{e}{m} \left(\delta \varphi(x) - \frac{e\delta n(x)}{C_q} \right) &= \int_0^x \left\langle v_1 \partial_x v_1 - (1 - \eta) \frac{n_1 v_1}{n_0 \tau} + \right. \\ &\quad \left. \nu \partial_x^2 \frac{n_1 v_1}{n_0} - \eta \frac{v_F^2}{2} \frac{n_1 \partial_x n_1}{n_0^2} - \eta \nu \frac{n_1 \partial_x^2 v_1}{n_0} \right\rangle_t dx'. \quad (47) \end{aligned}$$

The photovoltage ΔU defined in Eq. (20) can be expressed in terms of the first-order solution in Eq. (36) as

$$\begin{aligned} \frac{\Delta U}{V_b} &= \sum_j a_j(\omega) \left(\left| \frac{v_1^{(j)}(0, \omega)}{s_1} \right|^2 - \left| \frac{v_1^{(j)}(\ell_j, \omega)}{s_1} \right|^2 \right) \\ &\quad + \sum_j b_j(\omega) \frac{s_j^2}{s_1^2} \left(\left| \frac{n_1^{(j)}(0, \omega)}{n_0} \right|^2 - \left| \frac{n_1^{(j)}(\ell_j, \omega)}{n_0} \right|^2 \right), \quad (48) \end{aligned}$$

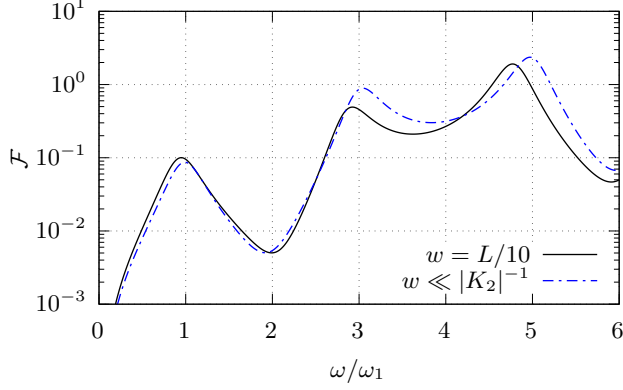


FIG. 3. Dimensionless photovoltage \mathcal{F} , defined in Eq. (51), for a GaAs FET with a single top gate centered in $x_0 = L/2$, as a function of the frequency ω of the radiation. The solid (dash-dotted) line shows the evaluation of Eq. (48) [Eq. (52)] for a gate of width $w = L/10$ (vanishing width). The electron liquid parameters are: $n_0 = 10^{11} \text{ cm}^{-2}$, $\tau = 20 \text{ ps}$, $\nu = 0$. The geometrical parameters are: $L = 10 \mu\text{m}$, $h_b = h_t = 100 \text{ nm}$, $\varepsilon_b = \varepsilon_t = 10$. With these parameters the frequency ω shown on the horizontal axis varies from 0 to $6\omega_1 \approx 700 \text{ GHz}$.

where we have introduced the functions

$$a_j(\omega) = 2 - \eta - \frac{\nu}{\tau} \left(\frac{1 + \omega^2 \tau^2}{s_j^2 + \omega^2 \nu \tau} + 2 \frac{s_j^2 + \omega^2 \nu \tau}{s_j^4 + \omega^2 \nu^2} \right), \quad (49)$$

$$b_j(\omega) = 1 - \eta \left(1 + \frac{v_F^2}{2s_j^2} \right) - \omega \nu \frac{\omega \tau - \omega \nu / s_j^2}{s_j^2 + \omega^2 \nu \tau}. \quad (50)$$

Finally, since the dependence of the photovoltage on the amplitude of the incoming radiation is rigorously second-order because of our perturbative procedure, it is convenient to introduce a dimensionless photovoltage function \mathcal{F} defined by

$$\mathcal{F}(\omega) \equiv \frac{\Delta U(\omega)}{V_b} \left(\frac{U_a}{2V_b} \right)^{-2}. \quad (51)$$

D. Approximate formula for a single top gate of negligible width

Let us focus on the case of a single top gate centered in x_0 , with negligible width, in order to provide an entirely analytical result for the photovoltage. The condition of negligible width translates precisely into the inequality $|K_2(\omega)w| \ll 1$. In order to apply the local capacitance approximation, we also need $|K_{1,2}(\omega)h_{b,t}| \ll 1$, and $h_{b,t} \ll w \ll L$. For the sake of simplicity we set $\nu = 0$. Calculating the coefficients A_1, \dots, A_6 of the first-order solution in this limit, we derive the following analytical formula for the photovoltage

$$\mathcal{F}(\omega) = \left[\frac{C_2 C_t}{C_b (C_b + C_t)} \frac{\omega w}{s_1} \right]^2 \frac{1}{\cosh(2\kappa L) + \cos(2kL)} \left\{ (2-\eta) [\cosh(2\kappa(L-x_0)) + \cos(2k(L-x_0))] - \left[1 - \eta \left(1 + \frac{v_F^2}{2s_2^2} \right) \right] \times \right. \\ \left. [\cos(2kx_0) \cosh(2\kappa(L-x_0)) + \cosh(2\kappa x_0) \cos(2k(L-x_0))] - \left[1 - \eta \left(1 + \frac{v_F^2}{2s_1^2} \right) \right] \alpha(\omega) [\cosh(2\kappa x_0) - \cos(2kx_0)] \right\}, \quad (52)$$

where, for $\nu = 0$, $\alpha(\omega) = \sqrt{1 + (\omega\tau)^{-2}}$, $k(\omega) = \text{Re } K_1(\omega) = \frac{\omega}{s_1} \sqrt{(\alpha(\omega) + 1)/2}$, and $\kappa(\omega) = \text{Im } K_1(\omega) = \frac{\omega}{s_1} \sqrt{(\alpha(\omega) - 1)/2}$.

In Fig. 3, we compare the photovoltage given by the approximate analytical formula in Eq. (52) to the numerical evaluation of the general formula in Eq. (48). The approximate formula predicts that the photovoltage has peaks at the odd harmonics of the fundamental plasma frequency $\omega_1 \equiv \pi s_1 / 2L$, as in the original result by DS [31]. The numerical results shows that this result is qualitatively correct, although it also predicts a redshift of the peak frequencies on the order of $\sim 10\%$ for the second and third resonances, and a sizeable modulation of the peak amplitude (please notice the logarithmic scale of the vertical axis). The analytical formula reported in

Eq. (52) can thus be used to obtain a reliable prediction of the expected photovoltage as a function of the gate position, if its width is much smaller than the channel.

V. GEOMETRICAL EFFECTS ON THE PHOTOVOLTAGE

We now turn to the investigation of the dependence of the photovoltage on several geometrical parameters of the FET. Figs. 4 and 5 show the profile of the photovoltage for a device with a single top gate based on GaAs and SLG, respectively. The color scale represents the amplitude of the dimensionless function \mathcal{F} , with the radiation frequency ω and the gate width w (in units of L) on the

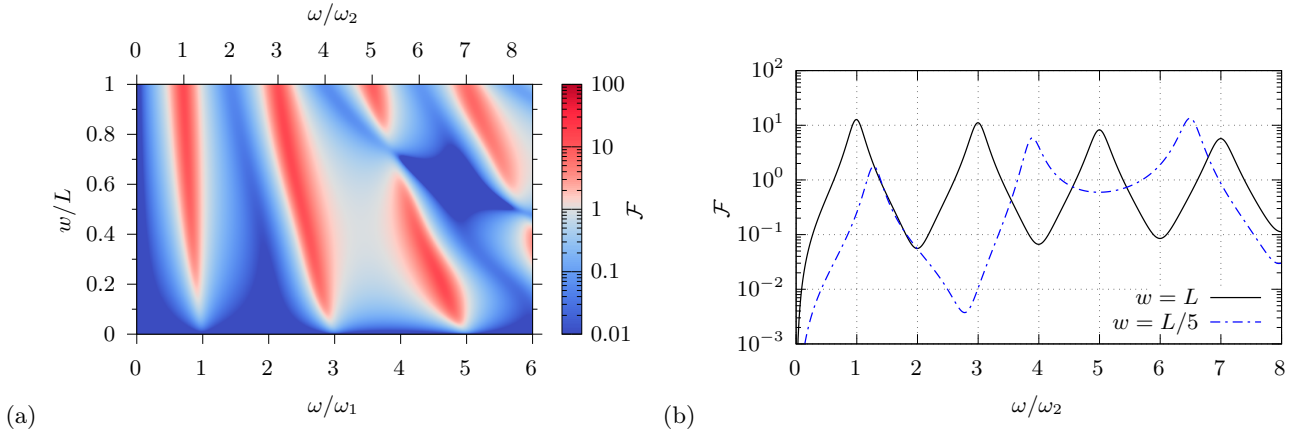


FIG. 4. (a) Dimensionless photovoltage \mathcal{F} for a GaAs FET with a single top gate centered in $x_0 = L/2$, as a function of the frequency ω and the gate width w . (b) Horizontal cuts of the profile shown in (a) for $w = L$ (solid line) and $w = L/5$ (dash-dotted line). The electron liquid parameters are: $n_0 = 10^{11} \text{ cm}^{-2}$, $\tau = 50 \text{ ps}$, $\nu = 100 \text{ cm}^2/\text{s}$. The geometrical parameters are the same as in Fig. 3. These parameters correspond to the fundamental plasma frequencies $\omega_1 \approx 113 \text{ GHz}$, $\omega_2 \approx 80 \text{ GHz}$.

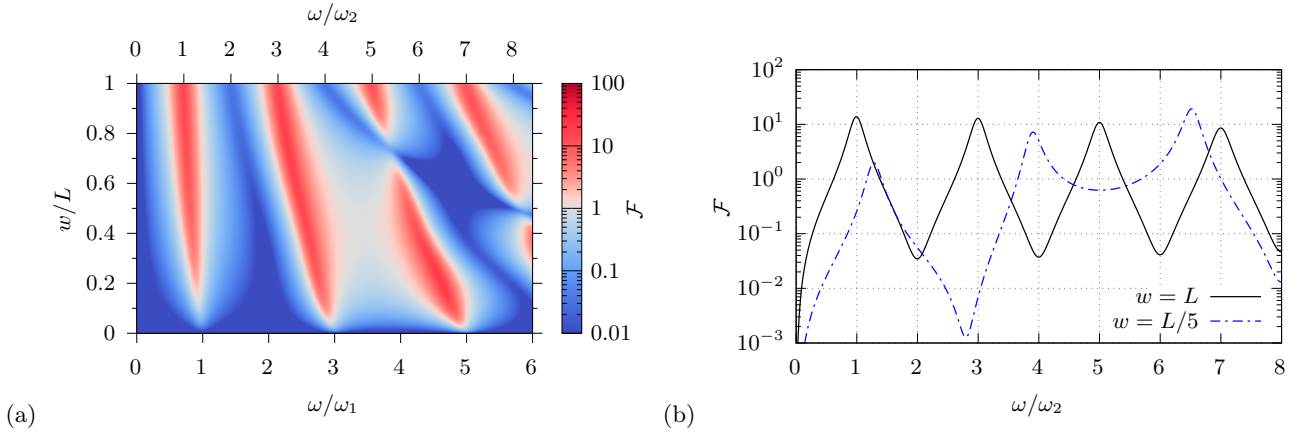


FIG. 5. Same as in Fig. 4, but for SLG FET, with $n_0 = 10^{12} \text{ cm}^{-2}$, $\tau = 5 \text{ ps}$, $\nu = 500 \text{ cm}^2/\text{s}$, $L = 10 \mu\text{m}$, $h_b = h_t = 100 \text{ nm}$, $\varepsilon_b = \varepsilon_t = 3$, corresponding to $\omega_1 \approx 1.16 \text{ THz}$ and $\omega_2 \approx 827 \text{ GHz}$.

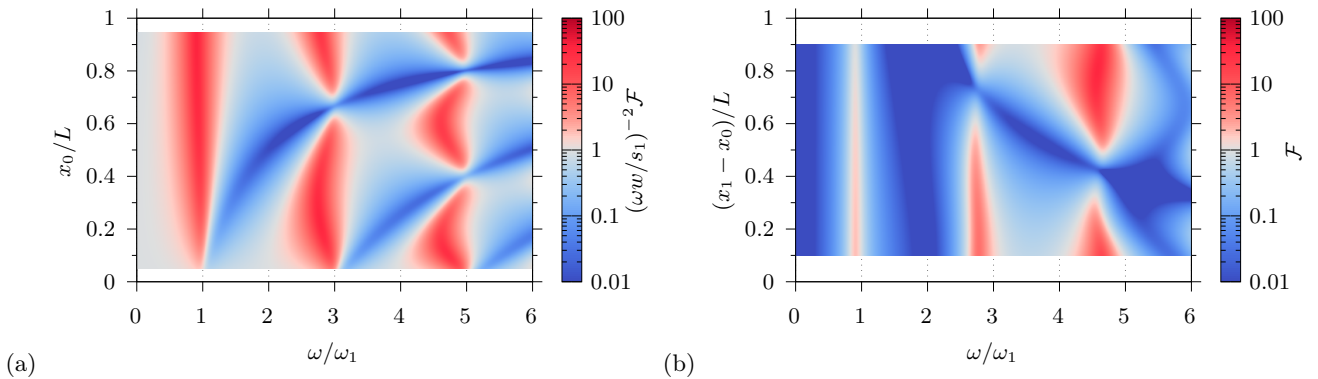


FIG. 6. (a) Dimensionless photovoltage for a GaAs FET with a single top gate of width $w = L/10$, as a function of the frequency ω and the gate position x_0 . For the sake of a clearer image we collect the factor $(\omega w/s_1)^2$. The parameters are the same of Fig. 4. (b) Dimensionless photovoltage for GaAs, with two gates of width $w = L/10$, positioned in x_0 and x_1 symmetrically with respect to the center of the channel, as a function of the frequency ω and the distance between the two gates. The other parameters are the same of Fig. 4.

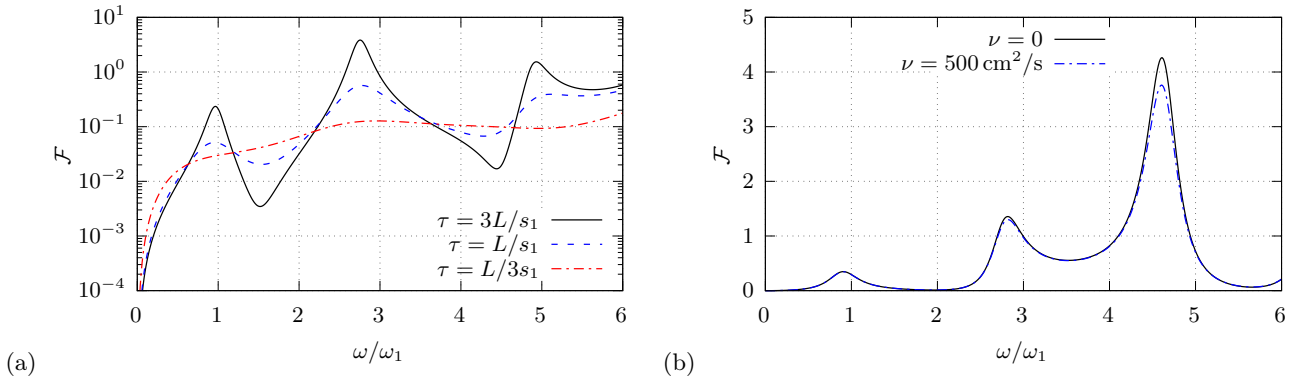


FIG. 7. (a) Dimensionless photovoltage for GaAs, with a single gate of width $L/10$ centered in $x_0 = L/3$, as a function of the frequency ω , for several values $\tau = 3L/s_1$ (solid line), L/s_1 (dashed line), $L/3s_1$ (dash-dotted line). The parameters are the same of Fig. 4, therefore $L/s_1 \approx 14$ ps. (b) Dimensionless photovoltage for SLG, with a single gate of width $w = L/5$ centered in $x_0 = L/2$, as a function of the frequency ω for two values of the viscosity $\nu = 0$ (solid line) and $\nu = 500 \text{ cm}^2/\text{s}$ (dash-dotted line). The other parameters are the same of Fig. 5, except $\tau = 2$ ps.

horizontal and vertical axes, respectively. The gate width goes from a negligible value (bottom) to the full length of the channel (top). Correspondingly, the horizontal axis shows the ratio between the radiation frequency and the plasma frequency $\omega_1 \equiv \pi s_1/2L$ of the ungated regions (bottom), or the plasma frequency $\omega_2 \equiv \pi s_2/2L$ of the gated region (top). This double horizontal axis makes it clear that the maxima of the photovoltage smoothly shift from the odd multiples of ω_1 when $w \ll L$ to the odd multiples of ω_2 when $w \lesssim L$. This transition shows that the resonant frequency of the photodetector crucially depends on the width of the top gate, and that it is approximately determined by an average of the plasma wave speeds in the SGRs and DGR. In the limit in which the top gate occupies the whole length of the channel, the photovoltage of Eq. (48) reproduces the results of Refs. [31, 33].

Fig. 6(a) shows the photovoltage for a device based on GaAs with a single top gate of finite width $w = L/10$, as a function of the frequency ω on the horizontal axis and the position x_0 of the center of the gate on the vertical axis. Since the gate has a finite width w , the value x_0 varies between $w/2$ and $L - w/2$. The color scale represents the amplitude of the dimensionless function \mathcal{F} multiplied by a scaling factor to improve visibility of the profile over the entire parameter range. This is due to the fact that for a top gate of small width the photovoltage is proportional to $(\omega w/s_1)^2$, as we showed in the analytical formula (52). Familiar maxima of the photovoltage appear at the odd multiples of the fundamental plasma frequency [cfr. Fig. 4], but they are intercalated by structures of minima which drift in frequency as the position x_0 of the gate is tuned. This result shows that a random positioning of the gate could potentially be very detrimental to the efficiency of the photodetection device, if it happens to match one of the minima.

We therefore conclude that a careful calculation of the photovoltage for given gate position and given width is necessary prior to fabrication to optimize the efficiency of the device. This conclusion, which has been overlooked so far in the previous theoretical analyses and the experimental fabrication of devices, is the main result of this Article. The probability that a top gate is inefficiently positioned is larger if higher harmonics need to be excited to achieve photodetection, since it appears that the number of minima in the n th harmonic response profile is $n - 1$. We also notice that tuning the gate position induces a sensible red-shift of the resonance. However, since the value of fundamental plasma frequency is tuned with the *bottom* gate by changing the average electron density, this red-shift can be easily corrected to achieve frequency-resolved detection. Fig. 6(b) shows the dimensionless photovoltage with $N = 2$ top gates. Here, for the sake of definiteness, we choose to consider the simplest extension to the one-gate case, and we fix the position of the two gates in a symmetric fashion. We notice that the maxima of the photovoltage still roughly appear at the odd multiples of the fundamental plasma fre-

quency, demonstrating the underlying robustness of the wave-mixing effect at the basis of the DS photodetection scheme. However, we see substantial modulation of the resonance profile, both in maximum amplitude and in width. Moreover, a complex structure of minima intersects the peaks, once more highlighting the importance of a precise calculation supporting the device fabrication stage.

Finally, in Fig. 7 we investigate the effects of the two source of dissipation in the dynamics of the electron liquid, namely (a) momentum relaxation due to impurity scattering and (b) electron viscosity. Fig. 7(a) shows that the resonance amplitude is regulated by the dimensionless parameter $\tau s_1/L$. Indeed, fixing the device geometry and the electronic density, the momentum relaxation time τ determines the resonant response, since the peaks height grows with the square of the mobility of the sample. Fig. 7(b) shows that the peaks at higher harmonics are damped more strongly due to a finite viscosity. This is due to the fact that the viscosity term in the Navier–Stokes equation is a second-order derivative in space, thus proportional to $\nu K_j^2(\omega) \sim \nu \omega^2/s_j^2$. In particular, the quality factor is $s_1 \tau^*/L$, where $1/\tau^* = 1/\tau + \nu K_1^2$ [31]. Thus, the quality of the resonance decreases at higher harmonics.

VI. CONCLUSIONS

In this Article, we have presented a generalization of the Dyakonov–Shur photodetection theory to the case of dual-gated field-effect transistors in which one or several top gates occupy a limited portion of the channel. Surprisingly, this configuration, although common in experimental practice [36, 37], has not been theoretically analyzed so far. We have provided such analysis and demonstrated that it is much-needed during the fabrication stage. Indeed, a sub-optimal placement of the gates can lead to substantially underperforming devices.

We have derived an expression for the photovoltage [Eq. (48)] both for devices where the electron dispersion is parabolic, as in the case of n -doped GaAs quantum wells, and devices where it is linear, as in the case of single-layer graphene. Both the width and position of a single top gate affect the way plasma waves interfere, inducing a modulation of the resonances, as shown in Figs. 4 and 6. We have also provided a compact analytical formula [Eq. (52)] for the photovoltage, valid in the limit of a negligible single top gate, which can be used to quickly estimate the optimal gate position.

ACKNOWLEDGMENTS

This work was supported by “National Centre for HPC, Big Data and Quantum Computing,” under the National Recovery and Resilience Plan (NRRP), Mission

4 Component 2 Investment 1.4 funded from the European Union – NextGenerationEU. M.P. is supported by the MUR - Italian Ministry of University and Research under the “Research projects of relevant national interest - PRIN 2020” - Project No. 2020JLZ52N (“Light-matter interactions and the collective behavior of quantum 2D materials, q-LIMA”) and by the European Union under

grant agreement No. 101131579 - Exqiral and No. 873028 - Hydrotronics. Views and opinions expressed are however those of the author(s) only and do not necessarily reflect those of the European Union or the European Commission. Neither the European Union nor the granting authority can be held responsible for them.

-
- [1] R. W. Boyd, *Nonlinear Optics, 4th Edition* (Academic Press, Cambridge, 2020).
- [2] Y. R. Shen, *The Principles of Nonlinear Optics* (John Wiley & Son, New York, 1984).
- [3] M. Polini and A. K. Geim, Viscous electron fluids, *Phys. Today* **73**, 28 (2020).
- [4] D. A. Bandurin, I. Torre, R. Krishna Kumar, M. Ben Shalom, A. Tomadin, A. Principi, G. H. Auton, E. Khestanova, K. S. Novoselov, I. V. Grigorieva, L. A. Ponomarenko, A. K. Geim, and M. Polini, Negative local resistance caused by viscous electron backflow in graphene, *Science* **351**, 1055 (2016).
- [5] J. Crossno, J. K. Shi, K. Wang, X. Liu, A. Harzheim, A. Lucas, S. Sachdev, P. Kim, T. Taniguchi, K. Watanabe, T. A. Ohki, and K. C. Fong, Observation of the Dirac fluid and the breakdown of the Wiedemann-Franz law in graphene, *Science* **351**, 1058 (2016).
- [6] R. Krishna Kumar, D. A. Bandurin, F. M. D. Pellegrino, Y. Cao, A. Principi, H. Guo, G. H. Auton, M. Ben Shalom, L. A. Ponomarenko, G. Falkovich, K. Watanabe, T. Taniguchi, I. V. Grigorieva, L. S. Levitov, M. Polini, and A. K. Geim, Superballistic flow of viscous electron fluid through graphene constrictions, *Nat. Phys.* **13**, 1182 (2017).
- [7] P. Gallagher, C.-S. Yang, T. Lyu, F. Tian, R. Kou, H. Zhang, K. Watanabe, T. Taniguchi, and F. Wang, Quantum-critical conductivity of the Dirac fluid in graphene, *Science* **364**, 158 (2019).
- [8] A. I. Berdyugin, S. G. Xu, F. M. D. Pellegrino, R. K. Kumar, A. Principi, I. Torre, M. Ben Shalom, T. Taniguchi, K. Watanabe, I. V. Grigorieva, M. Polini, A. K. Geim, and D. A. Bandurin, Measuring Hall viscosity of graphene’s electron fluid, *Science* **364**, 162 (2019).
- [9] J. A. Sulpizio, L. Ella, A. Rozen, J. Birkbeck, D. J. Perello, D. Dutta, M. Ben-Shalom, T. Taniguchi, K. Watanabe, T. Holder, R. Queiroz, A. Principi, A. Stern, T. Scaffidi, A. K. Geim, and S. Ilani, Visualizing Poiseuille flow of hydrodynamic electrons, *Nature* **576**, 75 (2019).
- [10] M. J. H. Ku, T. X. Zhou, Q. Li, Y. J. Shin, J. K. Shi, C. Burch, L. E. Anderson, A. T. Pierce, Y. Xie, A. Hamo, U. Vool, H. Zhang, F. Casola, T. Taniguchi, K. Watanabe, M. M. Fogler, P. Kim, A. Yacoby, and R. L. Walsworth, Imaging viscous flow of the Dirac fluid in graphene, *Nature* **583**, 537 (2020).
- [11] C. Kumar, J. Birkbeck, J. A. Sulpizio, D. Perello, T. Taniguchi, K. Watanabe, O. Reuven, T. Scaffidi, A. Stern, A. K. Geim, and S. Ilani, Imaging hydrodynamic electrons flowing without Landauer–Sharvin resistance, *Nature* **609**, 276 (2022).
- [12] B. A. Braem, F. M. D. Pellegrino, A. Principi, M. Rössli, C. Gold, S. Hennel, J. V. Koski, M. Berl, W. Dietsche, W. Wegscheider, M. Polini, T. Ihn, and K. Ensslin, Scanning gate microscopy in a viscous electron fluid, *Phys. Rev. B* **98**, 241304(R) (2018).
- [13] L. V. Ginzburg, C. Gold, M. P. Rössli, C. Reichl, M. Berl, W. Wegscheider, T. Ihn, and K. Ensslin, Superballistic electron flow through a point contact in a Ga[Al]As heterostructure, *Phys. Rev. Research* **3**, 023033 (2021).
- [14] A. C. Keser, D. Q. Wang, O. Klochan, D. Y. H. Ho, O. A. Tkachenko, V. A. Tkachenko, D. Culcer, S. Adam, I. Farrer, D. A. Ritchie, O. P. Sushkov, and A. R. Hamilton, Geometric control of universal hydrodynamic flow in a two-dimensional electron fluid, *Phys. Rev. X* **11**, 031030 (2021).
- [15] X. Wang, P. Jia, R.-R. Du, L. N. Pfeiffer, K. W. Baldwin, K. W. West, Hydrodynamic charge transport in GaAs/AlGaAs ultrahigh-mobility two-dimensional electron gas, *Phys. Rev. B* **106**, L241302 (2022).
- [16] A. Aharon-Steinberg, T. Völkl, A. Kaplan, A. K. Pariari, I. Roy, T. Holder, Y. Wolf, A. Y. Meltzer, Y. Myasoedov, M. E. Huber, B. Yan, G. Falkovich, L. S. Levitov, M. Hücker, and E. Zeldov, Direct observation of vortices in an electron fluid, *Nature* **607**, 74 (2022).
- [17] I. Torre, A. Tomadin, A. K. Geim, and M. Polini, Nonlocal transport and the hydrodynamic shear viscosity in graphene, *Phys. Rev. B* **92**, 165433 (2015).
- [18] B. N. Narozhny, I. V. Gornyi, M. Titov, M. Schütt, and A. D. Mirlin, Hydrodynamics in graphene: Linear-response transport, *Phys. Rev. B* **91**, 035414 (2015).
- [19] L. Levitov and G. Falkovich, Electron viscosity, current vortices and negative nonlocal resistance in graphene, *Nat. Phys.* **12**, 672 (2016).
- [20] B. N. Narozhny, I. V. Gornyi, A. D. Mirlin, and J. Schmalian, Hydrodynamic Approach to Electronic Transport in Graphene, *Ann. Phys.* **529**, 1700043 (2017).
- [21] H. Guo, E. Ilseven, G. Falkovich, and L. S. Levitov, Higher-than-ballistic conduction of viscous electron flows, *Proc. Natl. Acad. Sci.* **114**, 3068 (2017).
- [22] A. Shytov, J. F. Kong, G. Falkovich, and L. Levitov, Particle Collisions and Negative Nonlocal Response of Ballistic Electrons, *Phys. Rev. Lett.* **121**, 176805 (2018).
- [23] P. Ledwith, H. Guo, A. Shytov, and L. Levitov, Tomographic Dynamics and Scale-Dependent Viscosity in 2D Electron Systems, *Phys. Rev. Lett.* **123**, 116601 (2019).
- [24] L. Fritz, J. Schmalian, M. Müller, and S. Sachdev, Quantum critical transport in clean graphene, *Phys. Rev. B* **78**, 085416 (2008).
- [25] M. Müller, J. Schmalian, and L. Fritz, Graphene: A Nearly Perfect Fluid, *Phys. Rev. Lett.* **103**, 025301 (2009).
- [26] G. F. Giuliani and G. Vignale, *Quantum Theory*

- of the *Electron Liquid* (Cambridge University Press, Cambridge, 2005).
- [27] Q. Li and S. Das Sarma, Finite temperature inelastic mean free path and quasiparticle lifetime in graphene, *Phys. Rev. B* **87**, 085406 (2013).
- [28] M. Polini and G. Vignale, The quasiparticle lifetime in a doped graphene sheet, in *No-nonsense Physicist: An overview of Gabriele Giuliani's work and life*, edited by M. Polini, G. Vignale, V. Pellegrini, and J. K. Jain (Edizioni della Normale, Pisa, 2016) p. 107. Also available as [arXiv:1404.5728](https://arxiv.org/abs/1404.5728).
- [29] M. Dyakonov and M. Shur, Shallow water analogy for a ballistic field effect transistor: New mechanism of plasma wave generation by dc current, *Phys. Rev. Lett.* **71**, 2465 (1993).
- [30] M. I. Dyakonov and M. S. Shur, Choking of electron flow: A mechanism of current saturation in field-effect transistors, *Phys. Rev. B* **51**, 14341 (1995).
- [31] M. Dyakonov and M. Shur, Detection, mixing, and frequency multiplication of terahertz radiation by two-dimensional electronic fluid, *IEEE Trans. Electron Devices* **43**, 380 (1996).
- [32] M. I. Dyakonov and M. S. Shur, Plasma wave electronics: novel terahertz devices using two dimensional electron fluid, *IEEE Trans. Electron Devices* **43**, 1640 (1996).
- [33] A. Tomadin and M. Polini, Theory of the plasma-wave photoresponse of a gated graphene sheet, *Phys. Rev. B* **88**, 205426 (2013).
- [34] A. Tomadin, M. Carrega, and M. Polini, Microscopic theory of plasmon-enabled resonant terahertz detection in bilayer graphene, *Phys. Rev. B* **103**, 085426 (2021).
- [35] W. Knap, M. Dyakonov, D. Coquillat, F. Teppe, N. Dyakonova, J. Łusakowski, K. Karpierz, M. Sakowicz, G. Valusis, D. Seliuta, I. Kasalynas, A. Fatimy, Y. M. Meziani, and T. Otsuji, Field Effect Transistors for Terahertz Detection: Physics and First Imaging Applications, *J. Infrared Millim. Terahertz Waves*, **30**, 1319 (2009).
- [36] L. Vicarelli, M. S. Vitiello, D. Coquillat, A. Lombardo, A. C. Ferrari, W. Knap, M. Polini, V. Pellegrini, and A. Tredicucci, Graphene field-effect transistors as room-temperature terahertz detectors, *Nat. Mater.* **11**, 865 (2012).
- [37] D. Spirito, D. Coquillat, S. L. De Bonis, A. Lombardo, M. Bruna, A. C. Ferrari, V. Pellegrini, A. Tredicucci, W. Knap, and M. S. Vitiello, High performance bilayer-graphene terahertz detectors, *Appl. Phys. Lett.* **104**, 061111 (2014).
- [38] A. Tredicucci and M. S. Vitiello, Device Concepts for Graphene-Based Terahertz Photonics, *IEEE J. Sel. Top. Quantum Electron.* **20**, 130 (2014).
- [39] D. A. Bandurin, D. Svintsov, I. Gayduchenko, S. G. Xu, A. Principi, M. Moskotin, I. Tretyakov, D. Yagodkin, S. Zhukov, T. Taniguchi, K. Watanabe, I. V. Grigorieva, M. Polini, G. N. Goltsman, A. K. Geim, and G. Fedorov, Resonant terahertz detection using graphene plasmons, *Nat. Commun.* **9**, 5392 (2018).
- [40] F. H. L. Koppens, T. Mueller, Ph. Avouris, A. C. Ferrari, M. S. Vitiello, and M. Polini, Photodetectors based on graphene, other two-dimensional materials and hybrid systems, *Nat. Nanotechnol.* **9**, 780 (2014).
- [41] E. M. Lifshitz and L. P. Pitaevskii, *Course of Theoretical Physics*, Vol. 10: *Physical Kinetics* (Butterworth-Heinemann, Oxford, 1981).
- [42] B. N. Narozhny, Hydrodynamic approach to two-dimensional electron systems, *La Rivista del Nuovo Cimento* **45**, 661 (2022).
- [43] S. Rudin, Non-linear plasma oscillations in semiconductor and graphene channels and application to the detection of terahertz signals, *Intl. J. High Speed Electron. Syst.* **20**, 567 (2011).
- [44] D. Svintsov, V. Vyurkov, S. Yurchenko, T. Otsuji, and V. Ryzhii, Hydrodynamic model for electron-hole plasma in graphene, *J. Appl. Phys.* **111**, 083715 (2012).
- [45] L. D. Landau and E. M. Lifshitz, *Course of Theoretical Physics*, Vol. 6: *Fluid Mechanics* (Pergamon, Oxford, 1987) Second Edition.
- [46] A. Principi, G. Vignale, M. Carrega, and M. Polini, Bulk and shear viscosities of the two-dimensional electron liquid in a doped graphene sheet, *Phys. Rev. B* **93**, 125410 (2016).
- [47] M. I. Katsnelson, *The Physics of Graphene* (Cambridge University Press, Cambridge, 2020) Second Edition.
- [48] G. L. Yu, R. Jalil, B. Belle, A. S. Mayorov, P. Blake, F. Schedin, S. V. Morozov, L. A. Ponomarenko, F. Chiappini, S. Wiedmann, U. Zeitler, M. I. Katsnelson, A. K. Geim, K. S. Novoselov, and D. C. Elias, Interaction phenomena in graphene seen through quantum capacitance, *Proc. Natl. Acad. Sci. U.S.A.* **110**, 3282 (2013).